Solar-light-driven rapid water disinfection by ultrathin magnesium titanate/carbon nitride hybrid photocatalyst: Band structure analysis and role of reactive oxygen species

Zhifeng Jiang[a,b,1], Bo Wang[b,c,1], Yan Li[d,1], Ho Shing Chan[b], Hongli Sun[b], Tianqi Wang[b], Huaming Li[a], Shouqi Yuan[a], Michael K.H. Leung[e], Anhuai Lu[d,**], Po Keung Wong[b,f,*]

[a] Institute for Energy Research, Jiangsu University, Zhenjiang, 212013, China
[b] School of Life Sciences, The Chinese University of Hong Kong, Shatin, New Territories, Hong Kong, China
[c] Department of Chemistry, The Chinese University of Hong Kong, Shatin, New Territories, Hong Kong, China
[d] The Key Laboratory of Orogenic Belts and Crustal Evolution, Beijing Key Laboratory of Mineral Environmental Function, School of Earth and Space Sciences, Peking University, Beijing 100871, China
[e] Ability R&D Energy Research Centre, School of Energy and Environment, City University of Hong Kong, Hong Kong, China
[f] Institute of Environmental Health and Pollution Control, School of Environmental Science & Engineering, Guangdong University of Technology, Guangzhou 510006, China

ARTICLE INFO

ABSTRACT

Novel and cost-effective Z-scheme 2D/2D MgTi$_2$O$_5$/g-C$_3$N$_4$ hybrid was synthesized by *in situ* growth of MgTi$_2$O$_5$ on the g-C$_3$N$_4$ nanosheets. The photocatalytic activity of as-prepared hybrid was investigated using bacteria disinfection. The results indicated that the composite exhibited enhanced *E. coli* inactivation under visible light (VL) irradiation, with the complete inactivation of 7 log10 cfu/mL of cells reduction within 3 h, while the pristine g-C$_3$N$_4$ and MgTi$_2$O$_5$ almost showed no cell reduction under the same condition. The destruction of bacterial cell was investigated by fluorescence microscopic images and transmission electron microscopy analysis. The optimum photoactivity could be attributed to 1) the short charge transport distance and large interface contact area of the 2D/2D structure, 2) the efficient charge separation and spatially separated reductive and oxidative active sites originated from Z-scheme system. This work could shed lights on the design and fabrication of 2D/2D Z-scheme system for VL driven water disinfection.

1. Introduction

Microbial contamination in drinking water has always threatened the health of human beings, the safety of water and food production. The traditional antibacterial strategies, like ozonation disinfection and chlorination, are often chemically and operationally intensive, which strongly limited their application [1–4]. Heterogeneous photocatalysis has been recognized as an effective alternative strategy for the water disinfection due to the utilization of solar energy and environmental friendship with almost no formation of disinfection by-product. Consequently, much effort has been devoted to design effective, stable and low-cost materials for water disinfection [5–8].

MgTi$_2$O$_5$, a kind of alkali titanates, is known as an important indirect wide-band-gap semiconductor, and has attracted increasing attention due to its low-cost, high chemical stability, positive conduction band and unique layered crystal structure [9,10]. However, it is mainly active in the ultraviolet wavelength range due to its wide bandgap of ˜3.4 eV, and thus only 3–5% of the solar spectrum can be utilized. In addition, the high recombination rate of electrons and holes shall lead to the low overall photocatalytic efficiency. To address these issues, the development of efficient and robust photocatalysts for accelerating the water disinfection is of extremely urgent [11–13].

With the aim of utilizing solar energy, constructing heterojunction is an effective strategy to extend the photo responsive range of MgTi$_2$O$_5$ materials and efficiently improve charge separation and transfer [14,15]. Especially, the construction of all-solid-state direct Z-scheme system, mimicking the natural photosynthesis system, can not only boost the spatial separation efficiency of photoinduced electron-hole pairs, but also well preserve strong redox ability of two different redox sites [16–19]. For example, Zhu and co-workers reported the assembly

* Corresponding author at: School of Life Sciences, The Chinese University of Hong Kong, Shatin, New Territories, Hong Kong, China.
** Corresponding author.
E-mail addresses: ahlu@pku.edu.cn (A. Lu), pkowng@cuhk.edu.hk (P.K. Wong).
[1] Equal contribution.

of Z-scheme 2D heterostructure consisting of black phosphorus (BP) and $BiVO_4$. The $BP/BiVO_4$ composite showed enhanced photocatalytic activity toward water splitting into H_2 and O_2 because its reduction and oxidation reactions occurred on BP and $BiVO_4$, respectively [20]. Yu's group fabricated a ternary $Ag_2CrO_4/g-C_3N_4/GO$ composite photocatalyst for photocatalytic CO_2 reduction into methanol and methane by employing Ag_2CrO_4 as photosensitizer and GO as co-catalyst. The photocatalytic experimental results indicated that the ternary composites exhibited an enhanced CO_2 conversion activity as comparison with that of pristine $g-C_3N_4$ due to its broad light absorption, higher CO_2 adsorption and more powerful photogenerated electrons and holes derived from direct Z-scheme structure [21]. In addition, the emerging 2D/2D heterojunctions have opened new shine in photocatalysis owing to the significant advantages of the distinct "face-to-face" contact with large interface area and enhanced interfacial charge separation and transfer between layers [22–25].

Recently, 2D graphitic carbon nitride ($g-C_3N_4$) with π-conjugated system has been explored as one of the most promising metal-free photocatalysts in the field of various photocatalytic applications due to its appropriate band structure, easy availability, highly thermal/chemical stability and relatively low toxicity [26–31]. However, its photocatalytic efficiency is still limited due to the fast recombination of its photoinduced charge carriers. Combining $g-C_3N_4$ with other semiconductors to achieve spatial separation of charge carriers is an effective way to improve its photocatalytic efficiency. For example, Jing and co-workers prepared red $P/g-C_3N_4$ hybrid by introducing ultra-small red P crystals onto the surface of $g-C_3N_4$ using chemical-vapor-deposition (CVD) strategy and showed significantly enhanced photocatalytic activity toward hydrogen production [32].

Herein, we demonstrated a facile strategy for the synthesis of direct all-solid-state Z-scheme photocatalyst by assembling $MgTi_2O_5$ onto the $g-C_3N_4$ nanosheets and applied it under visible light to inactivate *Escherichia coli*. The photocatalytic experimental results showed that the Z-scheme $MgTi_2O_5/g-C_3N_4$ (MTO/CN) exhibited enhanced *E. coli* inactivation under visible light irradiation, while the pristine $g-C_3N_4$ and $MgTi_2O_5$ almost showed no cell reduction under the same condition. The disinfection activity of MTO/CN can be further improved when applying AM1.5 as light source, which is higher than most of the previously reported $g-C_3N_4$ based photocatalysts. The reactive oxygen species (ROS) roles were investigated. The Z-scheme mechanism was verified by electron spin resonance (ESR) analysis. It is envisaged that the Z-scheme system based on a 2D/2D hybrid composite will be an effective and viable solution for practical wastewater disinfection.

2. Experimental section

2.1. Preparation of g-C₃N₄ nanosheets

The $g-C_3N_4$ nanosheets were obtained based on our previous strategy [16]. Ten g of urea in a crucible with a cover were heated to 500 °C at a heating rate of 1 °C/min in a tube furnace for 3 h in air. The resulted yellow powder was washed with distilled water and absolute ethanol for several times to move any residual alkaline species adsorbed on the surface, and then dried at 60 °C for 24 h.

2.2. Preparation of MgTi₂O₅/g-C₃N₄ (MTO/CN) composites

In typical synthesis of MTO/CN composites, 0.3 g of $g-C_3N_4$ was added into ethylene glycol (30 mL) and then placed in an ultrasonic bath for 30 min to disperse the $g-C_3N_4$. Then, $Mg(CH_3COO)_2 \cdot 4H_2O$ (3.2 g) and $Ti(OC_4H_9)_4$ (1.7 mL) were added to the above mixture, followed by stirring at room temperature for 30 min. The result homogeneous suspension was transferred into a Teflon-lined autoclave (50 mL), followed by hydrothermal treatment at 180 °C for 24 h. The resulted products were centrifuged, washed with water/ethanol several times and dried at 60 °C overnight to remove the water/absolute

ethanol. Finally, the dry samples were calcined at 600 °C for 2 h with a constant heating rate of 2 °C min^{-1} to obtain MTO/CN composites. Pure $MgTi_2O_5$ (MTO) was prepared in the absence of $g-C_3N_4$. MTO/CN-1 and MTO/CN-2 were prepared in the presence of 0.15 and 0.45 g of $g-C_3N_4$, respectively.

2.3. Characterization

The components of as-prepared samples were analyzed by X-ray diffraction (XRD) using D8 Advance X-ray diffractometer (Bruker AXS GmbH, Germany) equipped with Cu-Kα radiation (λ = 1.5406 Å), employing a scanning rate of 0.02° s^{-1} in the 2θ range from 10 to 80°. The morphology and particle size of the products were examined by transmission electron microscopy (TEM) which was recorded on a JEOL-JEM-2010 (JEOL, Japan) operating at 200 kV. HAADF-STEM imaging was performed on a FEI Tecnai F20 microscope working at 200 kV. The optical properties of the samples were analyzed by UV–Vis diffuse reflectance spectroscopy (DRS) using a UV–Vis spectrophotometer. A Nicolet NEXUS470 Fourier transform infrared spectroscopy (FTIR) was applied to obtain Fourier transform infrared spectra. X-ray photoelectron spectroscopy (XPS) analysis was measured on an ESCALAB MK X-ray photoelectron spectrometer. The PL spectra of the samples were obtained by a QuantaMaster & TimeMaster Spectrofluorometer (QuantaMaster™40, USA).

2.4. Photoelectrochemical measurements

The electrochemical measurements were carried out in a three-electrode quartz cells using a computer-controlled electrochemical workstation (CHI660D, Shanghai Chenhua Instrument Company, China). Pt wire was used as the counter electrode and saturated calomel electrodes (SCE) as the reference electrode. The working electrode was obtained according to the following process: 5 mg of the as-prepared catalysts and 20 μL of Nafion solution (5 wt%) were dispersed in a 1 mL mixed solvent, which contains isopropanol and water (1:3 v/v) by sonication to form a homogeneous catalyst colloid. Then, 100 μL of the catalyst colloid was spread on the pretreated FTO (1.0 × 1.0 cm^{-2}), and dried in air at room temperature to form photocatalysts modified FTO. A 300 W Xe arc lamp with 400 nm cutoff filter was utilized as the light source in the photoelectrochemical measurements.

2.5. Photocatalytic inactivation process

The photocatalytic performances of the as-obtained catalysts were investigated by inactivation of *E. coli* using a 300 W Xenon lamp (PLS-SXE300C, PerfectLight Technology Co., Ltd. China) with a 400 nm ultraviolet cutoff filter as light source. The light intensity is 1000 W/m^2. Firstly, 25 mg catalysts were uniformly dispersed in 50 mL 0.9% NaCl solution by ultra-sonication for 2 min, followed by the addition of certain amount of bacterial suspension (~10^7 colony forming units per milliliter, cfu/mL). A water cooling system was used to maintain the temperature at 37 °C throughout the experiment. 1 mL of the mixed solution was collected at different time intervals and serially diluted with sterilized saline solution (0.9% NaCl). After that, 0.1 mL of the diluted solution was uniformly spread onto Nutrient Agar (Lab M, U.K.) plates. Finally, the plates were incubated at 37 °C for 18 h to determine the survival cell numbers. Light control and dark control (without light) were conducted in parallel to study whether photolysis or photocatalysts alone could cause the cell death.

3. Results and discussion

3.1. Catalysts characterization

X-ray diffraction (XRD) patterns of as-prepared MTO/CN composite, $g-C_3N_4$ as well as MTO were obtained and shown in Fig. 1a. For pristine
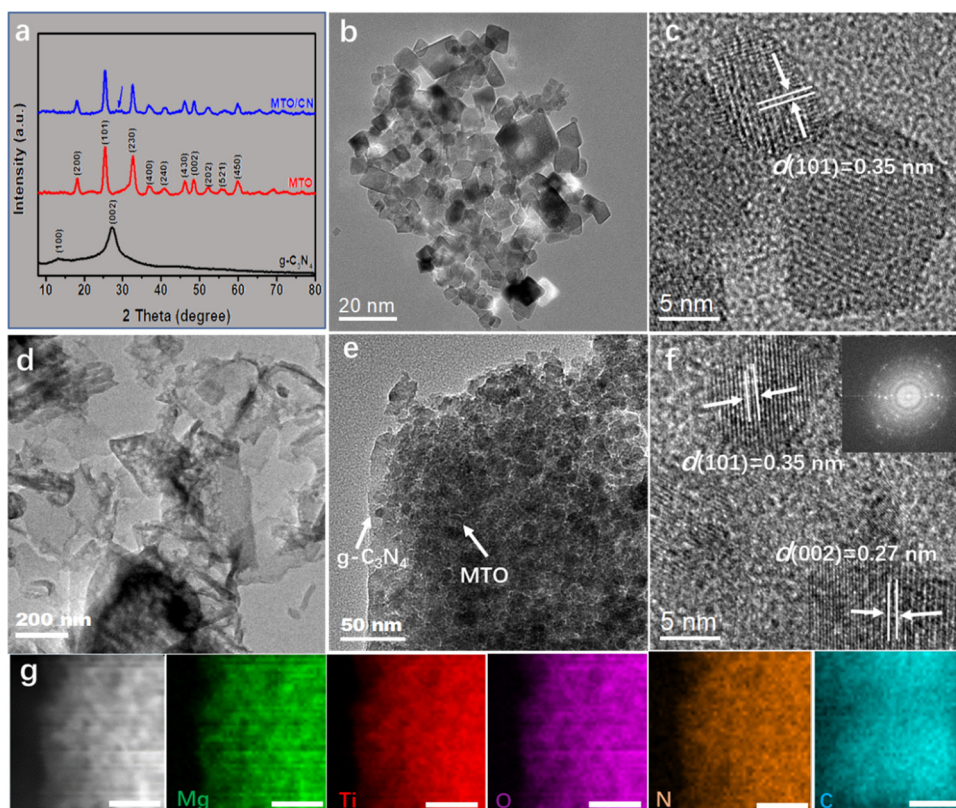
Fig. 1. XRD patterns (a) of as-prepared catalysts; TEM (b) and HRTEM (c) images of MTO; TEM (d) image of g-C₃N₄; TEM (e), HRTEM (f, inset: corresponding FFT) images, element mappings (g).
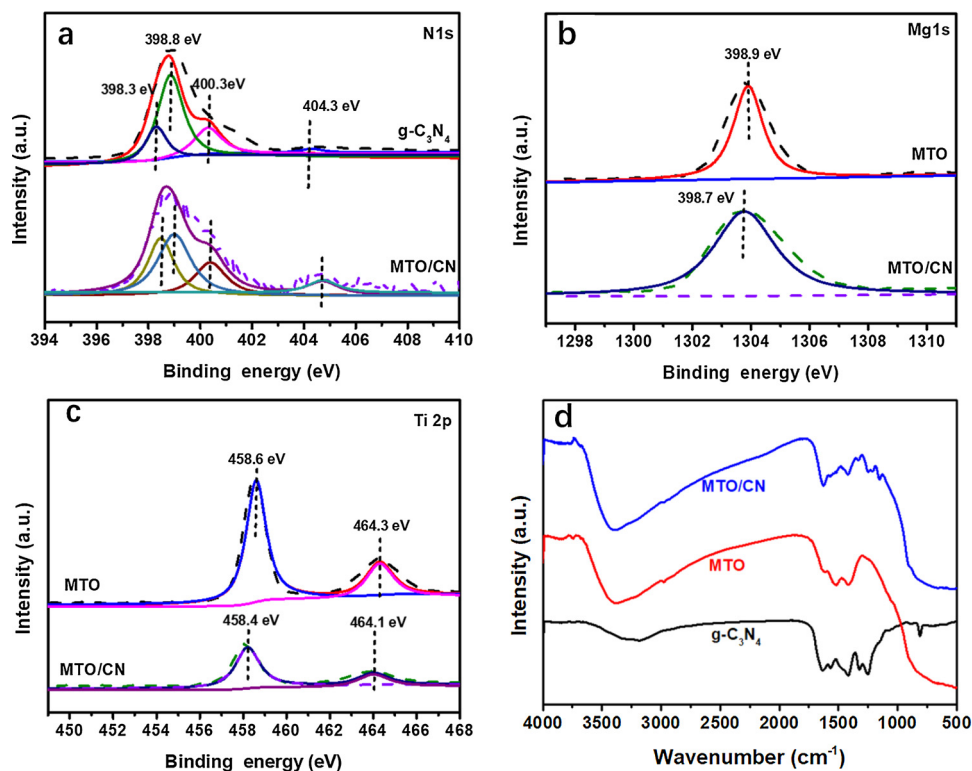

Fig. 2. High-resolution XPS spectra (a–c) of N 1s, Mg 1s and Ti 2p for the g-C₃N₄, MTO and MTO/CN composite; FT-IR spectra (d) of the as-prepared photocatalysts.

g-C$_3$N$_4$, two clear peaks at 13.0° and 27.3°, indexing as (100) and (002), respectively, can be clearly identified [33,34]. For pristine MTO, all diffraction peaks are well consistent with the standard pattern of pure orthorhombic phase MTO (JCPDS No. 35-0792) [9]. No other impurity peaks were detected. For MTO/CN composite, the characteristic peaks of MTO and g-C$_3$N$_4$ can be found in the composite, implying that the hybrid composite was successfully obtained. The morphological features and composition of the as-prepared samples were investigated by TEM, high-resolution transmission electron microscopy (HRTEM) and scanning transmission electron microscopy (STEM). As can be observed from Fig. 1b, MTO nanosheets with average size of 12 nm were successfully prepared. The HRTEM image in Fig. 1c demonstrates the high crystallization of MTO with crystal lattice of 0.35 nm corresponding to the (101) facet [9]. The flat layers in pristine g-C$_3$N$_4$ can be clearly identified from Fig. 1d, which is consistent with previous report [16]. As shown in Fig. 1e, large amount of small MTO nanosheets are densely distributed on the surface of g-C$_3$N$_4$, which is beneficial to interfacial charge. In addition, the HRTEM image (Fig. 1f) clearly shows the lattice spacing of 0.35 and 0.27 nm can be attributed to (101) and (002) facets of MTO (JCPDS No. 35-0792), respectively [10]. To further confirm the detail composition of the MTO/CN composite, STEM and the corresponding energy dispersive spectroscopy (EDS) elemental mapping images of the MTO/CN composite were carried out. The results demonstrate that elements Mg, Ti, O, C and N are homogeneously distributed on the surface of the entire composite matrices (Fig. 1g). Moreover, the EDS spectrum result is also consistent with the elemental mapping results (Fig. S1).

The high-resolution X-ray photoelectron spectroscopy (XPS) was further carried out to investigate the surface chemical compositions and chemical states of MTO/CN composite. The atomic ratio Mg, Ti, O, and N is 9:20:50:5 based on the XPS results. For C 1s spectrum (Fig. S2), two peaks concerning at 284.8 and 288.2 can be attributed to the C−C coordination of the surface adventitious carbon and corresponding to a C−N−C coordination of g-C$_3$N$_4$, respectively [35]. The N 1s spectrum of MTO/CN (Fig. 2a) can be separated into four peaks located at 398.5, 399, 400.5 and 404.5 eV, which can be ascribed to C−N−C groups, tertiary nitrogen N-(C)$_3$ groups, N−H groups and the signal of π excitations, respectively [36]. The N 1s peaks in the MTO/CN composite slightly shift to higher binding energy compared with g-C$_3$N$_4$, which can be attributed to the interfacial charge transfer between MTO and g-C$_3$N$_4$. [36] The XPS spectrum of Mg 1s (Fig. 2b) clearly shows a strong peak at 1303.7 eV, corresponding to Mg^{2+} species in MTO/CN. The Ti 2p spectral peaks (Fig. 2c) of MTO/CN composite are located at 458.4 and 464.1 eV, which are the typical peaks of Ti^{4+} [37]. Meanwhile, binding energies of Mg 1s and Ti 2p in the MTO/CN composite exhibit negative shift by 0.2 eV as comparison to pristine MTO sample, further indicating the strong interaction between MTO and g-C$_3$N$_4$ nanosheets. The XPS results demonstrate that the as-prepared MTO/CN is not a simple physical mixture but a heterostructure with strong interaction between MTO and g-C$_3$N$_4$, which is beneficial for the migration of photoinduced carriers. The composition of the as-prepared photocatalysts was further investigated by FTIR spectra (Fig. 2d). g-C$_3$N$_4$ shows three typical absorption regions at 3200–3600 cm^{-1}, 1600–1200 cm^{-1} and 806 cm^{-1} corresponding to H$_2$O/N−H band, CN heterocycles and the condensed CN heterocycles, respectively [38]. For pristine MTO, a broad peak located at around 600 cm^{-1} can be ascribed to Ti−O stretching mode [39]. The MTO/CN hybrid shows a combined main characteristic breathing modes of MTO and g-C$_3$N$_4$, further proves that the MTO/CN composite has been sucessfully prepared.

N$_2$ adsorption-desorption isotherms were performed to investigate the surface area (BET) and pore structure of the as-prepared samples (Fig. 3). The isotherms for the as-prepared samples are type IV according to the IUPAC classification, indicating the existence of mesoporous structure induced by stacking of layered materials [40]. This result can be further proved by the pore size distributions (located at 5–20 nm). The pristine g-C$_3$N$_4$ and MTO show BET surface area of

∼32.1 and 76.9 m^2/g, respectively. The BET surface area of MTO/CN hybrid composite reaches 85.9 m^2/g, which is higher than those of g-C$_3$N$_4$ and MTO. The bigger surface area may contribute to enhanced harvesting of light and more reactive active sites for photocatalytic reaction.

3.2. Photocatalytic inactivation of bacteria

Before investigating the photocatalytic activities of the as-prepared catalysts, we first evaluated the optical absorption properties of the samples. As can be observed from Fig. 4a, the absorption edge of pristine g-C$_3$N$_4$ is *ca.* 450 nm, which is consistent with previous report [29]. MgTi$_2$O$_5$ only absorbs UV light with a wavelength shorter than 365 nm. After combining with g-C$_3$N$_4$, the absorption range of the MTO/CN composite slightly shifts to a higher wavelength, which is potential for visible-light-driven (VLD) photocatalytic application. The photocatalytic performances of the as-prepared photocatalysts were evaluated by the inactivation of *E. coli* under visible light irradiation (Fig. 4b and c). The density of bacterial cell almost remains unchanged within 4 h in the dark control and visible irradiation in the absence of photocatalysts, suggesting no toxic effect on the bacteria as well as no photolysis of the bacterial cell under visible light irradiation alone (Fig. 4b). The viability of *E. coli* during the photocatalytic experiments with MTO/CN series composites and their single components (MTO and g-C$_3$N$_4$) were shown in Fig. 4c. Both MTO and g-C$_3$N$_4$ cannot inactivate of *E. coli* after 4 h irradiation. An approximate 7.4-log10 cfu/mL reduction of *E. coli* is obtained within 3.5 h when using MTO/CN-1 (m (MTO) = 0.6 g, m(CN) = 0.15 g) as photocatalyst. When we increase the CN amount in the hybrid of MTO/CN, 7.4- log10 of *E. coli* is completely inactivated by MTO/CN (m(MTO) = 0.6 g, m(CN) = 0.3 g) within 3 h. Further increasing the CN amount to 0.45 g (MTO/CN-2), a rapid decrease of the bacterial inactivation activity is observed. Only 3.2-log10 cfu/mL of *E. coli* is inactivated in the presence of MTO/CN-2 within 4 h under visible light irradiation. Suitable ratio of MTO to g-C$_3$N$_4$ exhibits the highest bacterial inactivation efficiency, which shall be explained by the reasonable heterojunction (in favorable for charge separation at the contacted interface) between MTO and g-C$_3$N$_4$ in the composites. The disinfection performance of physical mixture of MTO and g-C$_3$N$_4$ was investigated, in which the physical mixture of MTO and CN cannot inactivate of *E. coli*, further giving the evidence of formation of heterojunction. When the g-C$_3$N$_4$ content is above the optimal value, the efficient heterojunction interface may not increase significantly. In addition, the excessive g-C$_3$N$_4$ shall act as recombination center of photoinduced carriers, thus reducing the photocatalytic disinfection activity. The disinfection of *E. coli* by MTO/CN was also investigated under different light spectrum. The results indicated that the disinfection performance is further enhanced under the irradiation of full spectrum and simulated solar (Fig. 4d). The complete 7-log10 bacterial disinfection is obtained within 1 h, which is higher than most of the previously reported g-C$_3$N$_4$ based photocatalysts (Table S1). It is reported that photo-corrosion may occur after light irradiation, causing the deactivation of photocatalysts [41]. To get the stability information of the hybrid system, the recycling photocatalytic test of bacterial inactivation on the MTO/CN photocatalyst was performed. The results demonstrate that the photocatalytic performance of MTO/CN does not decline significantly after four cycles of *E. coli* inactivation under visible light irradiation (Fig. 4e), which suggesting that the as-prepared sample can be used as a stable photocatalyst for bacterial inactivation. Fig. S3 shows the XPS spectra of the MTO/CN composite which has been used for 4 recycling runs. No obvious difference can be observed from the XPS spectra before and after reaction, further demonstrating the stability of the as-prepared catalyst.

The cell membrane integrity variation of *E. coli* during the inactivation with MTO/CN composite was visually observed by fluorescent microscopy (Fig. 5a–d) and SEM (Fig. 5e–h). At the beginning of the photocatalytic treatment, all the healthy cells are stained
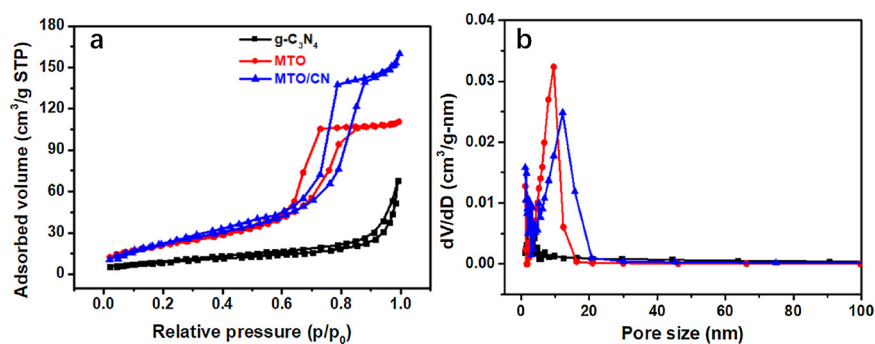
Fig. 3. N$_2$ adsorption-desorption isotherms (a) and pore size distribution curves (b) of the as-prepared photocatalysts.
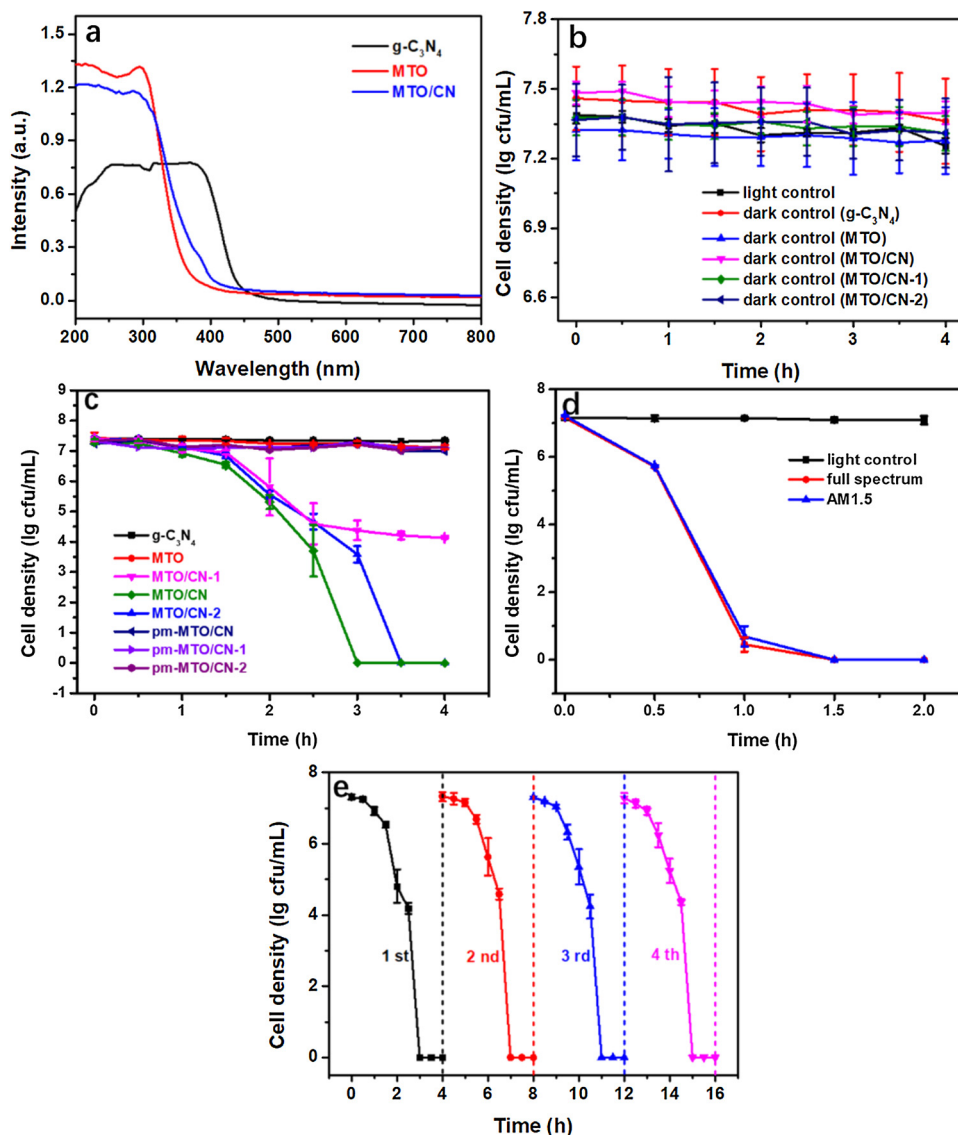

Fig. 4. Diffuse-reflectance spectroscopy (a), experimental controls (b), photocatalytic inactivation activity (c,d), and stability (e) of the as-prepared samples under visible light irradiation.

green (Fig. 5a) and exhibited intact and plump rod shape (Fig. 5e). After 1 h, a small portion of bacterial cells are stained red (Fig. 5b), and the MTO/CN particles are observed to attached and aggregated on the surface of the *E. coli* (Fig. 5f). The results indicates a loss of cell membrane integrity in the injured cells. With prolonged irradiation time, increased number of green fluorescent cells are replaced by the red cells (Fig. 5c). Moreover, blurred edges of the cell membranes are

observed (Fig. 5g), illustrating that most of the cell have lost the membrane integrity under the photocatalytic treatment. After being treated for 3 h, all bacterial cells are stained red (Fig. 5d) and the cell surfaces are wrinkled and broken (Fig. 5h), suggesting that the bacterial cells are further destroyed by the MTO/CN composite, and the cell integrity is totally lost, finally resulting in the cell death.

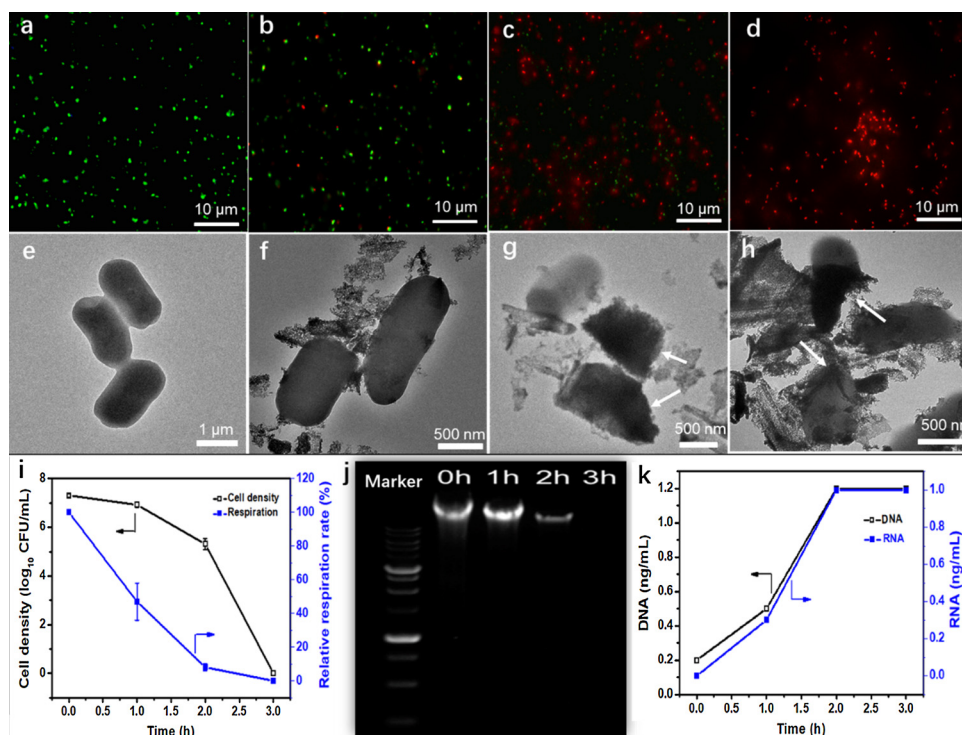Respiration is fundamental for cellular energy production through

Fig. 5. Fluorescence change and TEM images of *E. coli* cells being photocatalytically inactivated by the MTO/CN composite for (a, e) 0 h, (b, f) 1 h, (c, g) 2 h, and (d, h) 3 h; (i) cell density and relative respiration activity; (j) investigation of the leakage bacterial genomic DNA extracted from harvested cells (10^8 cfu/mL) during photocatalytic inactivation using agarose gel electrophoresis; (k) concentration of the leakage of DNA and RNA during the destruction of bacterial cells.

oxidative phosphorylation of substrate with oxygen as the final electron acceptor. [1] The respiration activity testing experimental results indicate that most of the bacterial cells have lost the activity within 2 h, and the complete inactivation is achieved at 3 h (Fig. 5i). To further investigate cell destruction level, the leakage of DNA and RNA contents was studied as the cells can self-repair and regrow even when their proteins are broken. As shown in Fig. 5j, the fluorescent intensity of genomic DNA decreased significantly after 2 h treatment, and fianlly disappeared after 3 h. The DNA and RNA concentration (Fig. 5k) was investigated using Nanodrop, and the results show that more and more nucleic acids are released to the suspension during the photocatalytic inactivation process. All these results demonstrate that the as-prepared catalyst can effectively destroy the bacteria cell.

3.3. Mechanism of photocatalytic bacterial inactivation

The reactive species trapping experiments were performed to investigate the key reactive species in the photocatalytic *E. coli* inactivation. The concentration of every scavenger was optimized to make sure the maximum scavenging effect while no toxic/inactivation effect to *E. coli* cells. As shown in Fig. 6a, the photocatalytic inactivation efficiencies are inhibited by leaps and bounds after the addition of TEMPOL (1 mM) and Fe-EDTA (0.1 mM) to capture $\cdot O_2^-$ and H_2O_2, respectively, suggesting that $\cdot O_2^-$ and H_2O_2 are the dominant reactive species in the visible light driven photocatalytic inactivation process. Holes (h$^+$) and $\cdot OH$ species are proved to play moderate roles in the inactivation process, as affirmed by the residual of 3.8 log10 cfu/mL and 1.2 log10 cfu/mL of *E. coli* cells when employing isopropanol (7.5 mM) and sodium oxalate (0.5 mM) to remove $\cdot OH$ and h$^+$, respectively. However, with the addition of 0.1 mM Cr(VI) to the photocatalytic sterilization reaction, the disinfection performance almost unchanged as compared to the bacterial inactivation without scavenger, indicating that electron is not the main reactive species in this inactivation process. To further identify the reactive oxygen radicals produced from MTO/CN system under visible light irradiation, the ESR technique with DMPO as a spin-trapping reagent was carried out. As can be clearly observed from Fig. 6b, no obvious $\cdot O_2^-$ signal can be detected in the ESR spectrum of MTO/CN under dark condition,

whereas the characteristic peaks (1: 1: 1: 1) of $\cdot O_2^-$ are detected in the methanol dispersion of the as-prepared MTO/CN under visible light irradiation, further confirming $\cdot O_2^-$ is the main reactive oxygen radical under this condition. We also found the DMPO-$\cdot OH$ signals (Fig. 6c) under visible light, demonstrating that $\cdot OH$ is reactive species in the inactivation process. As the main reactive species is $\cdot O_2^-$, we further investigated intracellular superoxide dismutase (SOD) because it can catalyze the dismutation of the $\cdot O_2^-$ to O_2 and/or H_2O_2 to protect the bacteria. The SOD activity drastically improved in the period of first 0.5 h, then decreased thereafter, suggesting that the antioxidant system takes effect in the existence of $\cdot O_2^-$ species at the beginning of the inactivation process and then damaged when most of the *E. coli* cells are broken. We also measured the peroxidation intermediate MDA, which can be used to evaluate the membrane oxidation degree. The MDA concentration increases at the initial 1.5 h, demonstrating that the lipid content is gradually oxidized, leading to the damage of cell membrane. As the MDA is a peroxidation intermediate, it can be further transferred to other final products. Thus, the MDA concentration decreases after 1.5 h (Fig. 6d). Taken together, these results suggest that the reactive species attack the bacterial cell and finally destroy the cell.

To better understand the mechanism of synergistic photocatalytic bacterial inactivation, the band energy alignment of the MTO/CN composites were determined by combining UV–vis DRS (Fig. 3a and Fig. 7a) Mott-Schottky plots (Fig. 7b) as well as valance band XPS (VB-XPS) analysis (Fig. 7c). Based on the UV–vis DRS spectra, the band gaps of the g-C$_3$N$_4$ and MTO can be calculated to be 2.7 and 3.4 eV, respectively, which are consistent with the previous reports [9,31]. The flatband potentials of g-C$_3$N$_4$ and MTO are determined to be −0.65 and −0.5 V *vs* NHE based on Mott-Schottky curves, respectively. The positive slopes of the Mott-Schottky plots indicates that both g-C$_3$N$_4$ and MTO are n-type semiconductors, which the fermi level (E$_f$) is close to flatband potential. The valance XPS spectra were used to evaluate the energy gap from valance band maximum (VBM) to the Fermi level (E$_f$) of semiconductors. As shown in Fig. 7c, the VBM positions of g-C$_3$N$_4$ and MTO are determined to be 2.3, and 3.0 eV below the Fermi level, respectively. As such, the VBM /conduction band maximum (CBM) positions of g-C$_3$N$_4$ and MTO can be calculated to be 1.65/−1.05 and 2.5/−0.9 eV, respectively (Fig. 7d). As shown in Fig. 7d, based on the
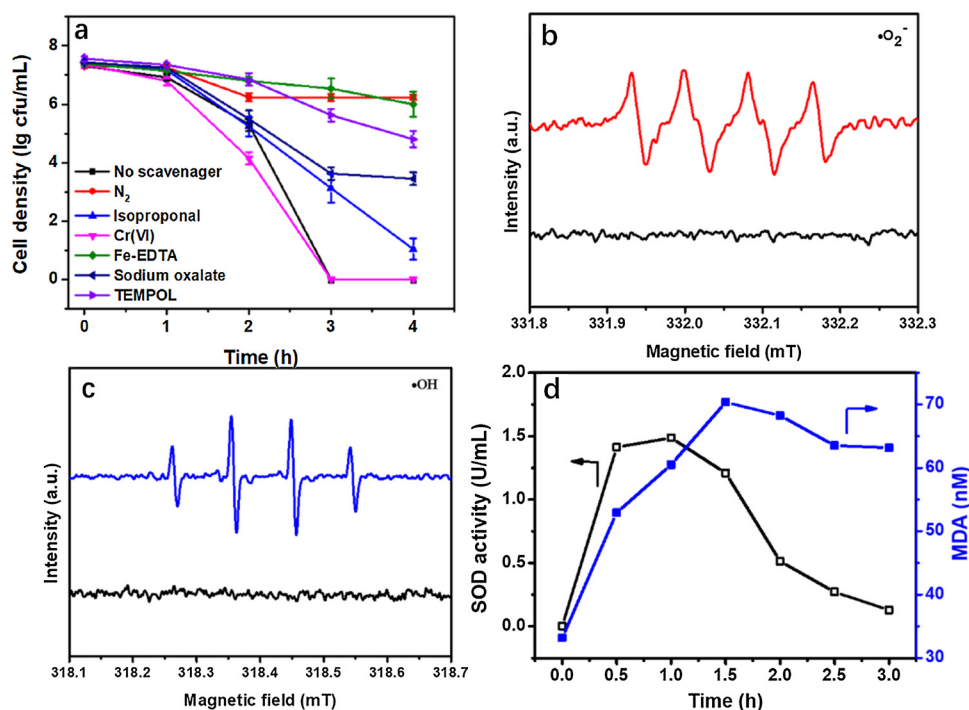
Fig. 6. Photocatalytic inactivation efficiency (a) against *E. coli* K-12 (10^7 cfu/mL, 50 mL) with addition of different scavengers (0.1 mM Cr(VI), 0.1 mM Fe-EDTA, 7.5 mM isopropanol, 0.5 mM sodium oxalate and 1 mM TEMPOL), respectively; ESR spectra of DMPO-$\cdot O_2^-$ (b) and DMPO-$\cdot$OH (c) in the presence of MTO/CN composite under visible light irradiation; MDA generation and SOD activity (d) during the photocatalytic disinfection of *E. coli*.
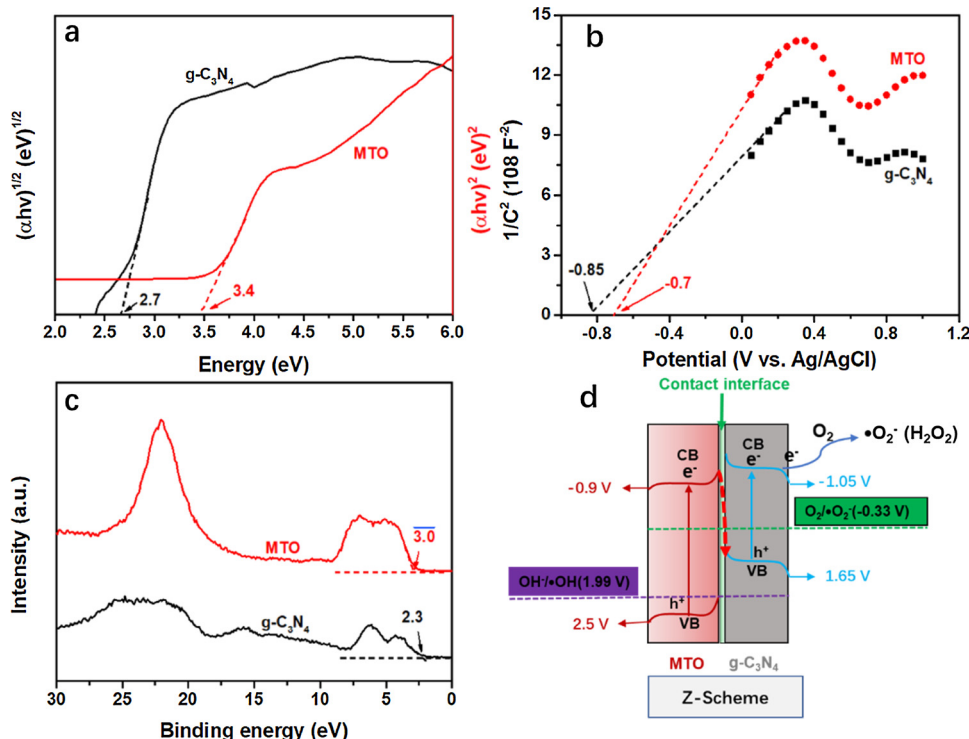

Fig. 7. Kubelka-Munk function transformed differential spectra (a), Mott-Schottky plot (b), valance band XPS spectra and energy band diagram of g-C_3N_4 and MTO.

traditional type-II heterojunction mechanism, the production of $\cdot$OH is forbidden because the VB potential of g-C_3N_4 (1.65 V *vs* NHE) is more negative than that of $OH^-/\cdot OH$ (1.99 V *vs* NHE). We still detect the $\cdot$OH species in the absence of oxygen confirms that the formation of $\cdot$OH in our system is original from the oxidation of H_2O/OH^- by holes. Meanwhile, as mentioned above (Fig. 6c), the MTO/CN composite can produce $\cdot$OH by using 5,5-dimethyl-1-pyrroline N-oxide (DMPO) as a spin trap under visible light irradiation, suggesting that the as-prepared hybrid follows the Z-scheme system rather than the traditional

heterojunction structure. The possible mechanism can be proposed in Fig. 8.

The charge separation ability of these as-prepared samples was investigated to understand the enhanced photocatalytic activity of Z-scheme MTO/CN composite *via* PEC experiments and PL test. As can be observed from Fig. 9a, the photocurrent of Z-scheme MTO/CN shows significant enhancement as comparison with MTO and g-C_3N_4 under several on/off cycles under visible light irradiation, indicating a promoted separation ability of the photoinduced carriers within Z-scheme

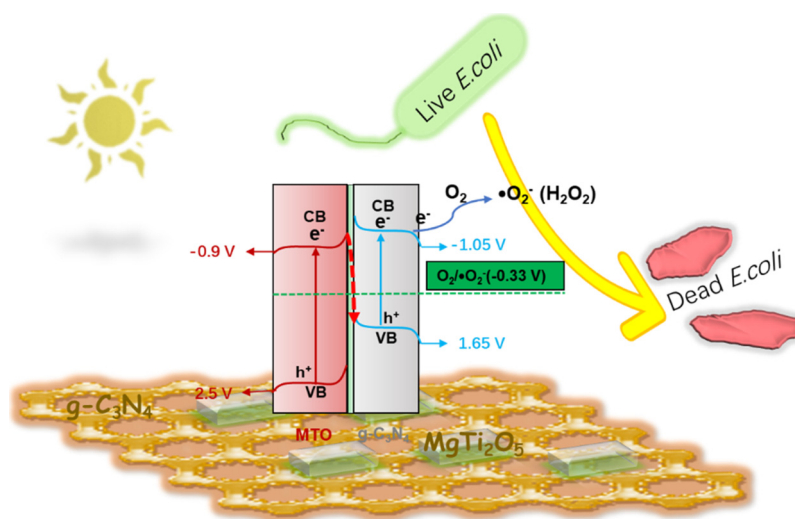**Fig. 8.** Proposed mechanism for the photocatalytic inactivation toward *E. coli* by Z-scheme MTO/CN composite.
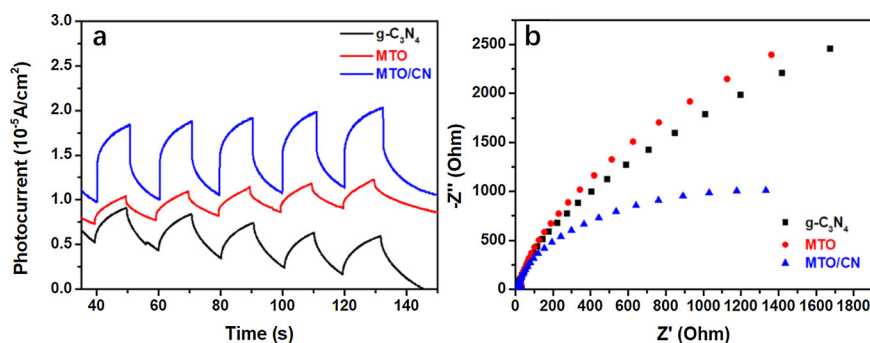

Fig. 9. Photocurrent density (a), Nyquist plots (b) of the as-prepared samples.

MTO/CN composite. Moreover, the Z-scheme MTO/CN composite shows an apparent smaller semicircle in Nyquist plots (Fig. 9b) compared to that of pristine C_3N_4 and MTO, indicating that the formation of Z-scheme structure can efficiently reduce the charge transfer resistances. The improved separation ability of the photogenerated electron-hole pairs of the sample MTO/CN could be further demonstrated by room temperature photo luminance measurements as illustrated in Fig. S4. A lower the PL emission intensity indicates a higher the separation efficiency of the photogenerated carriers. The main emission peak of $g-C_3N_4$ is centered at 468 nm, which can be attributed to the band-band PL phenomenon with the energy of light approximately equal to the band energy of $g-C_3N_4$. After combining with MTO, the PL intensity of the composite decreases dramatically, proving that the recombination of the carriers is greatly hindered. In conclude, the Z-scheme structure consists of MTO and $g-C_3N_4$ is beneficial to reduce charge transfer resistance, promote the charge separation, and thus improve the photocatalytic activity.

4. Conclusions

In summary, 2D/2D Z-scheme heterojunction was successfully prepared based on $MgTi_2O_5$ and $g-C_3N_4$ for visible light driven photocatalytic inactivation of *E. coli*. The MTO/CN composite shows enhanced inactivation activity in comparison to the pristine $g-C_3N_4$ and MTO under visible light irradiation. The improved photocatalytic activity can be ascribed to the following two factors: (1) the well-preserved strong redox ability, thus enhancing the charge separation efficiency, and (2) the unique 2D/2D heterojunction possesses large interface contact area and short charge transport distance, leading to the efficient electron transfer. This work provides new insights into the

design of 2D/2D all-solid-state Z-scheme photocatalysts for VLD water disinfection.

Declaration of interests

None.

Appendix A. Supplementary data

Supplementary material related to this article can be found, in the online version, at doi:https://doi.org/10.1016/j.apcatb.2019.117898.

References

[1] D. Xia, Z. Shen, G. Huang, W. Wang, J.C. Yu, P.K. Wong, Environ. Sci. Technol. 49 (2015) 6264.
[2] T. Wang, Z. Jiang, T. An, G. Li, H. Zhao, P.K. Wong, Environ. Sci. Technol. 52 (2018) 4774.
[3] D. Xia, H. Liu, Z. Jiang, T.W. Ng, W.S. Lai, T. An, W. Wang, P.K. Wong, Appl. Catal. B: Environ. 224 (2018) 541.

[4] H. Sun, H.Y. Yip, Z. Jiang, L. Ye, I.M.C. Lo, P.K. Wong, J. Mater. Chem. A 6 (2018) 4997.

[5] D. Xia, Y. Li, G. Huang, R. Yin, T. An, G. Li, H. Zhao, A. Lu, P.K. Wong, Water Res. 112 (2017) 236.

[6] D. Wu, S. Yue, W. Wang, T. An, G. Li, H.Y. Yip, H. Zhao, P.K. Wong, Appl. Catal. B 192 (2016) 35.

[7] W. Wang, Y. Yu, T. An, G. Li, H.Y. Yip, J.C. Yu, P.K. Wong, Environ. Sci. Technol. 46 (2012) 4599.

[8] K.M. Parker, T. Zeng, J. Harkness, A. Vengosh, W.A. Mitch, Environ. Sci. Technol. 48 (2014) 11161.

[9] Y. Qu, W. Zhou, Y. Xie, L. Jiang, J. Wang, G. Tian, Z. Ren, C. Tian, H. Fu, Chem. Commun. 49 (2013) 8510.

[10] N. Zhang, K. Zhang, W. Zhou, B. Jiang, K. Pan, Y. Qu, G. Wang, RSC Adv. 5 (2015) 106151.

[11] Q. Xu, B. Zhu, C. Jiang, B. Cheng, J. Yu, Sol. RRL 2 (2018) 1800006.

[12] P. Zhou, J. Yu, M. Jaroniec, Adv. Mater. 26 (2014) 4920.

[13] Z. Hu, Z. Shen, J.C. Yu, Environ. Sci. Technol. 51 (2017) 7076.

[14] P. Xia, B. Zhu, B. Cheng, J. Yu, J. Xu, ACS Sustain. Chem. Eng. (6) (2018) 965.

[15] S. Cao, B. Shen, T. Tong, J. Fu, J. Yu, Adv. Funct. Mater. 28 (2018) 1800136.

[16] Z. Jiang, W. Wan, H. Li, S. Yuan, H. Zhao, P.K. Wong, Adv. Mater. (2017) 1706108.

[17] Z. Zhang, J. Huang, Y. Fang, M. Zhang, K. Liu, B. Dong, Adv. Mater. 29 (2017) 1606688.

[18] H. Gao, P. Zhang, J. Zhao, Y. Zhang, J. Hua, G. Shao, Appl. Catal. B: Environ. 210 (2017) 297.

[19] Q. Yuan, D. Liu, N. Zhang, W. Ye, H. Ju, L. Shi, R. Long, J. Zhu, Y. Xiong, Angew. Chem. Int. Ed. 129 (2017) 4270.

[20] M. Zhu, Z. Sun, M. Fujitsuka, T. Majima, Angew. Chem. Int. Ed. 57 (2018) 2160.

[21] D. Xu, B. Cheng, W. Wang, C. Jiang, J. Yu, Appl. Catal. B: Environ. 231 (2018) 368.

[22] J. Ran, W. Guo, H. Wang, B. Zhu, J. Yu, S. Qiao, Adv. Mater. 30 (2018) 1800128.

[23] J. Low, S. Cao, J. Yu, S. Wageh, Chem. Commun. 50 (2014) 10768.

[24] X. Hong, J. Kim, S. Shi, Y. Zhang, C. Jin, Y. Sun, S. Tongay, J. Wu, Y. Zhang, F. Wang, Nat. Nanotechnol. 9 (2014) 682.

[25] C. Fu, Q. Luo, X. Li, J. Yang, J. Mater. Chem. A 4 (2016) 18892.

[26] G. Dong, L. Zhao, X. Wu, M. Zhu, F. Wang, Appl. Catal. B: Environ. 245 (2019) 459.

[27] L. Zhao, G. Dong, L. Zhang, Y. Lu, Y. Huang, ACS Appl. Mater. Interfaces 11 (2019) 10042.

[28] X. Wang, K. Maeda, A. Thomas, K. Takanabe, G. Xin, J. Carlsson, K. Domen, M. Antonietti, Nat. Mater. 8 (2009) 76.

[29] Z. Jiang, K. Qian, C. Zhu, H. Sun, W. Wan, J. Xie, H. Li, P. Wong, S. Yuan, Appl. Catal. B: Environ. 210 (2017) 194.

[30] D. Zheng, X. Cao, X. Wang, Angew. Chem. Int. Ed. 55 (2016) 11512.

[31] G. Zhang, Z. Lan, L. Lin, S. Lin, X. Wang, Chem. Sci. 7 (2016) 3062.

[32] L. Jing, R. Zhu, D.L. Phillips, J.C. Yu, Adv. Funct. Mater. (2017) 1703484.

[33] M. Zhu, S. Kim, L. Mao, M. Fujitsuka, J. Zhang, X. Wang, T. Majima, J. Am. Chem. Soc. 139 (2017) 13234.

[34] Y. Fang, X. Wang, Chem. Commun. 54 (2018) 5674.

[35] Z. Ding, X. Chen, M. Antonietti, X. Wang, ChemSusChem 4 (2011) 274.

[36] P. Xia, B. Zhu, B. Cheng, J. Yu, J. Xu, ACS Sustain. Chem. Eng. 6 (2018) 965.

[37] N. Zhang, Y. Qu, K. Pan, G. Wang, Y. Li, Nano Res. 9 (2016) 726.

[38] J. Yu, K. Wang, W. Xiao, B. Cheng, Phys. Chem. Chem. Phys. 16 (2014) 11492.

[39] Z. Jiang, K. Qian, C. Zhu, H. Sun, W. Wan, J. Xie, H. Li, P.K. Wong, S. Yuan, Appl. Catal. B: Environ. 210 (2017) 194.

[40] D. Xu, B. Cheng, W. Wang, C. Jiang, J. Yu, Appl. Catal. B: Environ. 231 (2018) 368.

[41] D. Xia, T.W. Ng, T. An, G. Li, Y. Li, H.Y. Yip, H. Zhao, A. Lu, P.K. Wong, Environ. Sci. Technol. 47 (2013) 11166.